Subcritical Destabilization of African Easterly Waves by Saharan Mineral Dust

TERRENCE R. NATHAN

Atmospheric Science Program, Department of Land, Air, and Water Resources, University of California, Davis, Davis, California

DUSTIN F. P. GROGAN

Department of Atmospheric and Environmental Sciences, University at Albany, State University of New York, Albany, New York

SHU-HUA CHEN

Atmospheric Science Program, Department of Land, Air, and Water Resources, University of California, Davis, Davis, California

ABSTRACT

A theoretical framework is presented that exposes the radiative–dynamical relationships that govern the subcritical destabilization of African easterly waves (AEWs) by Saharan mineral dust (SMD) aerosols. The framework is built on coupled equations for quasigeostrophic potential vorticity (PV), temperature, and SMD mixing ratio. A perturbation analysis yields, for a subcritical, but otherwise arbitrary, zonal-mean background state, analytical expressions for the growth rate and frequency of the AEWs. The expressions are functions of the domain-averaged wave activity, which is generated by the direct radiative effects of the SMD. The wave activity is primarily modulated by the Doppler-shifted phase speed and the background gradients in PV and SMD.

Using an idealized version of the Weather Research and Forecasting (WRF) Model coupled to an interactive dust model, a linear analysis shows that, for a subcritical African easterly jet (AEJ) and a background SMD distribution that are consistent with observations, the SMD destabilizes the AEWs and slows their westward propagation, in agreement with the theoretical prediction. The SMD-induced growth rates are commensurate with, and can sometimes exceed, those obtained in previous dust-free studies in which the AEWs grow on AEJs that are supercritical with respect to the threshold for barotropic–baroclinic instability. The clarity of the theoretical framework can serve as a tool for understanding and predicting the effects of SMD aerosols on the linear instability of AEWs in subcritical, zonal-mean AEJs.

1. Introduction

Vast plumes of Saharan mineral dust (SMD) aerosols punctuate the summertime circulation over North Africa (Karyampudi and Carlson 1988; Cuesta et al. 2009; Knippertz and Todd 2010). Originating from what Engelstaedter and Washington (2007) call hot spots,[1]

---

[1] Among the key dust hot spots are those located in Mali and Mauritania in West Africa and the Bodélé depression in Chad (Engelstaedter and Washington 2007).

Corresponding author e-mail: Terrence R. Nathan, trnathan@ucdavis.edu

the SMD is lofted into the atmosphere and transported from its North African seat of origin to affect regions as far away as the Caribbean and southeastern United States (Prospero and Carlson 1972; Prospero 1999). While in transit, the SMD absorbs, emits, and scatters radiation to affect the energy balance of the atmosphere and the surface below (Miller and Tegen 1998). In turn, the dust-induced change in the energy balance affects the atmospheric circulation and consequently the transport of SMD (Miller et al. 2014).

African easterly waves (AEWs) are among the circulation features that contribute to the mobilization and transport of SMD (Karyampudi and Carlson 1988; Jones et al. 2003; Knippertz and Todd 2010). Karyampudi

and Carlson (1988), for example, have noted that synoptic-scale outbreaks of SMD over North Africa have horizontal scales, frequencies of occurrence, and westward speeds that are similar to AEWs. Jones et al. (2003) used reanalysis data to characterize AEW activity and to drive the circulation in a transport model of SMD. They found that "approximately 20% of the dust entrainment into the atmosphere over a broad region of North Africa is associated with African easterly wave activity" and that "about 10%–20% of the seasonal variability of desert dust concentrations across the North Atlantic is related to easterly waves" (Jones et al. 2003, p. 3617).

Because the AEWs and SMD often operate over similar spatial and temporal scales, it is not surprising that the radiative effects of the SMD have been shown to affect the growth of AEWs (Jones et al. 2004; Jury and Santiago 2010; Ma et al. 2012; Grogan et al. 2016). For example, Jury and Santiago (2010) examined the effects of synoptic-scale plumes of SMD on AEWs located over the tropical northeast Atlantic. Based on a sample of objectively selected AEWs passing through environments characterized by high and low aerosol optical depth (AOD), Jury and Santiago (2010) used reanalysis and other data to show through statistical analysis that the SMD reduced the development of the AEWs. They attributed the reduced growth to the stabilization of the atmosphere caused, in part, by warming of the 850–600-hPa layer by the SMD field.

In contrast, Jones et al. (2004) found that a dust-modified environment increases the growth of AEWs. Using 22 yr of NCEP/NCAR meteorological reanalysis data and dust from a global transport model, Jones et al. (2004) provided observational evidence that the enhanced growth of AEWs over the Atlantic Ocean results from a reduction in static stability caused by dust-induced warming in the lower troposphere. Ma et al. (2012) used the WRF Model with prescribed dust profiles and, like Jones et al. (2004), found that the dust-radiative forcing reduces the static stability, producing an intensification of most, though not all, of the modeled AEWs.

Grogan et al. (2016) addressed the possible reasons why the SMD appears to weaken AEWs in some cases and strengthen them in others. Among the reasons cited by Grogan et al. (2016) is the SMD distribution, which can vary significantly over space and time. Over North Africa, for example, the SMD-laden air is hot and dry and generally well mixed in the boundary layer (Cuesta et al. 2009). But as the air migrates westward, eventually reaching the eastern Atlantic Ocean, it is undercut by the cool, moist marine layer to form an elevated layer of

relatively dry and dusty air, known as the Saharan air layer (Karyampudi and Carlson 1988).

Grogan et al. (2016) showed that the distribution of SMD, specifically its background gradients in the latitude–height plane, along with the location of critical surfaces and the African easterly jet (AEJ) structure, are key determinants for predicting how the SMD can affect the growth or decay of AEWs. These key determinants were identified from an analytically derived expression for the generation of eddy available potential energy (APE) by the direct radiative effects of SMD. Using the SMD-modified APE as an interpretive tool, Grogan et al. (2016) used the WRF-Dust model developed by Chen et al. (2015) to examine the effects of SMD on the linear stability characteristics of AEWs. Based on a realistic, zonal-mean AEJ that was *supercritical* to synoptic-scale waves (AEWs) in the SMD-free state, Grogan et al. (2016) showed that the SMD caused the fastest growing AEW to increase its linear growth rate from ~13%–90% for AODs ranging from 1.0 to 2.5. The maxima in energy generation and conversion were collocated and occurred where the meridional dust gradient was maximized near the critical layer, in agreement with the prediction obtained from the analytical expression for the generation of eddy APE by the SMD field.

Grogan et al. (2016) chose to examine the linear instability of a zonal-mean AEJ that was consistent with the summertime climatology over North Africa. Many studies, spanning more than 40 yr, have also chosen (supercritical) AEJs to explain the origin of AEWs in SMD-free atmospheres (Rennick 1976; Thorncroft and Hoskins 1994; Thorncroft 1995). Observations show, however, that the AEJ is characterized by pronounced intraseasonal variability (Afiesimama 2007; Leroux and Hall 2009); it is therefore likely that the AEJ will be *subcritical* with respect to synoptic-scale waves at various times during summer. We hypothesize that, at those times, the direct radiative effects of SMD can destabilize the waves, thus serving as a mechanism for the genesis of AEWs in subcritical background flows. If such is the case, then two questions immediately follow: Are the growth rates comparable to those obtained in supercritical background states? And what are the radiative–dynamical relationships that govern the SMD-induced instabilities?

To answer these questions, we develop in section 2 a theoretical framework that yields analytical expressions for the SMD-induced frequency and growth rate of synoptic-scale waves (AEWs) that are embedded in subcritical, zonal-mean background flows (AEJs). The expressions clearly show how the AEJ, AEW, and SMD

TABLE 1. List of symbols.

Variable	Definition
t; x, y, $z = -H \ln(p/p_0)$	Time; eastward, northward, and vertical directions
$\rho(z) = \rho_0 \exp(-z/H)$	Background reference density
H, p_0, ρ_0	Constant density scale height, sea level reference pressure, and density
$f_0 = 2|\Omega| \sin\theta_0$	Coriolis parameter; $|\Omega|$ is angular frequency of Earth; θ_0 is central latitude
$\beta = r_e^{-1} 2|\Omega| \cos\theta_0$	Northward gradient of the Coriolis parameter; r_e is Earth's radius
$S = N^2/f_0^2$	N^2 is Brunt–Väisälä frequency squared (assumed constant)
$\overline{u}(y, z)$, $\overline{T}(y, z)$, $\overline{\gamma}(y, z)$	Background zonal-mean wind, temperature, and SMD mass mixing ratio
$\phi(x, y, z, t)$, $\gamma(x, y, z, t)$	Perturbation streamfunction and SMD mass mixing ratio
$w(x, y, z, t)$	Perturbation vertical wind
$\dot{h}$, $\dot{d}$	SMD diabatic heating rate per unit mass and SMD depletion rate
$\overline{\Gamma}(y, z; \overline{\gamma})$, $\overline{D}(y, z; \overline{\gamma})$	SMD heating rate coefficient and SMD sedimentation rate coefficient
$\overline{\tau}(y, z)$, $\overline{T}_r(y, z)$	Mean aerosol optical depth and mean transmissivity
S_0, μ, σ_a	Solar constant, cosine of the solar zenith angle, and specific absorption coefficient
$\kappa = R_d/c_p$	R_d is gas constant for dry air; c_p is specific heat capacity at constant pressure
$\delta = \kappa/f_0 SH$	Constant parameter

structures combine to affect the propagation and growth of AEWs. The theoretical framework is then used as an interpretive tool for the WRF-Dust model stability results presented in section 3. The conclusions are presented in section 4 and discussed in light of observed AEWs over North Africa.

2. Theoretical framework

In this section, we derive analytical expressions for the dust-modified frequency, growth rate, and generation of APE for synoptic-scale waves (AEWs) over North Africa. Section 2a describes the radiative–dynamical model, while section 2b presents the mathematical development that yields the expressions for the frequency, growth rate, and generation of eddy APE. In section 2c, the expressions are analyzed for two cases: 1) the general case, which is valid for any zonal-mean, subcritical background flow; and 2) a simplified case, where the background fields are assumed to be slowly varying. This latter case serves two purposes. First, it clearly exposes how the SMD physics affects the growth of the model's AEWs, and, second, it extends Ghan (1989a), who examined the effects of an arbitrary trace absorber on the destabilization of Rossby waves, but who excluded latitudinal variations in the mean absorber mixing ratio.

a. Quasigeostrophic model

A theoretical framework that describes the subcritical destabilization of AEWs by the direct radiative effects of SMD is developed using a quasigeostrophic model atmosphere. The atmosphere is continuously stratified and confined to a zonally periodic, β-plane channel of width L and bounded from below by a flat, rigid boundary at $z = 0$. The background state is in radiative–dynamical equilibrium and characterized by a meridionally and vertically sheared zonal-mean current. The linear dynamics of this model atmosphere are governed by coupled equations for quasigeostrophic PV, SMD mass mixing ratio, and thermodynamic energy, which in log-pressure coordinates take the following form (Nathan and Li 1991):

$$\left(\frac{\partial}{\partial t} + \overline{u}\frac{\partial}{\partial x}\right)\left[\nabla^2\phi + \frac{1}{\rho}\frac{\partial}{\partial z}\left(\frac{\rho}{S}\frac{\partial\phi}{\partial z}\right)\right] + \beta_e\frac{\partial\phi}{\partial x} = \frac{\delta}{\rho}\frac{\partial}{\partial z}\left(\frac{\rho}{S}\dot{h}\right),$$

(2.1)

$$\left(\frac{\partial}{\partial t} + \overline{u}\frac{\partial}{\partial x}\right)\gamma + \frac{\partial\phi}{\partial x}\frac{\partial\overline{\gamma}}{\partial y} + w\frac{\partial\overline{\gamma}}{\partial z} = \dot{d}, \quad \text{and}$$

(2.2)

$$\left(\frac{\partial}{\partial t} + \overline{u}\frac{\partial}{\partial x}\right)\frac{\partial\phi}{\partial z} - \frac{\partial\phi}{\partial x}\frac{\partial\overline{u}}{\partial z} + \frac{N^2}{f_0}w = \frac{\kappa}{H}\dot{h},$$

(2.3)

where the overbar denotes a zonal average; $\phi(x, y, z, t)$ is the perturbation streamfunction, $\overline{u}(y, z)$ is the background zonal-mean current, and $\beta_e(y, z)$ is the northward gradient of quasigeostrophic PV, given by

$$\beta_e = \beta - \frac{\partial^2\overline{u}}{\partial y^2} - \frac{1}{\rho}\frac{\partial}{\partial z}\left(\frac{\rho}{S}\frac{\partial\overline{u}}{\partial z}\right);$$

(2.4)

$\gamma(x, y, z, t)$ and $\overline{\gamma}(y, z)$ are the perturbation and background SMD mass mixing ratios; $\dot{d}$ is the depletion rate of SMD; and $\dot{h}$ is the SMD-induced diabatic heating rate per unit mass. The remaining symbols in (2.1)–(2.4) are listed in Table 1.

The SMD depletion rate is modeled by sedimentation, which can be written as

$$\dot{d} = \overline{D}\gamma,$$

(2.5)

where $\overline{D} < 0$ is a constant and independent of dust particle size, assumptions that are relaxed in the WRF-Dust model to be described in section 3a.

For our analytical analysis, we consider the absorption of shortwave radiation by the SMD, excluding the effects of scattering and longwave emission. Calculations from the WRF-Dust model show that the daily averaged shortwave absorption alone captures the *qualitative* aspects of the dust effects on the circulation, though the daily averaged scattering and longwave emission are important to accurately measuring the *quantitative* effects. With this in mind, the SMD diabatic heating rate due to shortwave absorption can be written as follows (see appendix A):

$$\dot{h} = \overline{\Gamma}\gamma, \qquad (2.6)$$

where

$$\overline{\Gamma}(y, z; \overline{\gamma}) = S_0 \sigma_a \rho \exp(-\overline{\tau}). \qquad (2.7)$$

We refer to $\overline{\Gamma}$ as the "transmissivity parameter," since it is proportional to the zonal-mean transmissivity, $\overline{T}_r = \exp(-\overline{\tau})$. Here, S_0 is the solar constant, σ_a is the specific absorption coefficient, and $\overline{\tau}(y, z)$ is the zonal-mean AOD, given by

$$\overline{\tau} = \frac{1}{\mu} \int_z^\infty \rho \sigma_a \overline{\gamma} \, dz', \qquad (2.8)$$

where μ is the cosine of the solar zenith angle.

For the horizontal boundary conditions, we impose periodicity in the zonal direction and the kinematic boundary condition at the channel sidewalls. This latter condition requires that the meridional velocity, $\partial\phi/\partial x$, vanish at $y = \pm L/2$. At the lower boundary, $z = 0$, we require $w = 0$ and apply (2.3). At the upper boundary, we apply a radiation condition, which demands that the upward energy flux, $\rho\overline{w\phi}$, remain bounded as $z \to \infty$. These boundary conditions, together with (2.1)–(2.8), constitute a closed system governing the SMD-modified linear dynamics of synoptic-scale waves over North Africa.

b. Frequency, growth rate, and generation of eddy APE

Analytical expressions for the frequency, growth rate, and generation of eddy APE of the analytically modeled AEWs are obtained by assuming that the SMD diabatic heating rate is small and measured by the non-dimensional parameter $\varepsilon \ll 1$ such that $\dot{h} \to \varepsilon\dot{h}$. If we choose $\varepsilon = O(0.1)$, then the small heating rate assumption is consistent with the magnitude of the SMD heating rates obtained by Ma et al. (2012) and Grogan et al.

(2016). Both studies have shown using different modeling approaches that the SMD can increase the eddy kinetic energy of AEWs by ~10%–15%.

The detailed derivation of the frequency and growth rate is given in appendix B, with the salient aspects presented next. Solutions to (2.1)–(2.3) are sought in the form

$$(\phi, \gamma, w) = \sum_{n=0}^N \varepsilon^n(\phi_n, \gamma_n, w_n) \exp ik[x - (c_0 + \varepsilon c_1 + \ldots)t] + *, \qquad (2.9)$$

where $\phi_n(y, z)$, $\gamma_n(y, z)$, and $w_n(y, z)$ are the amplitudes of the respective wave fields, k is the zonal wavenumber, $c_n = c_{nr} + ic_{ni}$ is the (complex) phase speed, and the asterisk denotes the complex conjugate of the preceding term. Insertion of (2.9) into (2.1)–(2.8) yields a sequence of equations in powers ε. The zeroth-order balance yields adiabatic free wave solutions with amplitude structures $\phi_0(y, z)$, $\gamma_0(y, z)$, and $w_0(y, z)$, and real phase speed c_0. At zeroth order, the perturbation SMD is simply a passive tracer that is advected by the wave and zonal-mean flow; it is given by

$$\gamma_0 = (\overline{c}_0 + ik^{-1}\overline{D})^{-1} \left[-\phi_0 \frac{\partial\overline{\gamma}}{\partial y} + \frac{f_0}{N^2} \left(\overline{c}_0 \frac{\partial\phi_0}{\partial z} - \phi_0 \frac{\partial\overline{u}}{\partial z} \right) \frac{\partial\overline{\gamma}}{\partial z} \right], \qquad (2.10)$$

where $\overline{c}_0 = (\overline{u} - c_0)$ is the Doppler-shifted phase speed. We assume that $\overline{c}_0 > 0$, an assumption that is verified in section 3 based on an observationally representative subcritical background state.

At $O(\varepsilon)$, the SMD-induced diabatic heating effects enter as a forcing that projects onto the linear operator, which, if not removed, would invalidate the expansion (2.9). Thus, to ensure the validity of (2.9), we apply the solvability condition described in appendix B, which yields the following expressions for the SMD-modified frequency and growth rate:

$$kc_{1r} = \frac{1}{A_w} \int_{-L/2}^{L/2} \int_0^\infty \frac{\overline{D}}{k} \frac{\rho}{\rho_0} \Lambda F \, dz' \, dy' \quad \text{and} \qquad (2.11a)$$

$$kc_{1i} = \frac{1}{A_w} \int_{-L/2}^{L/2} \int_0^\infty \frac{\rho}{\rho_0} \Lambda \overline{c}_0 F \, dz' \, dy', \qquad (2.11b)$$

where

$$\Lambda = \delta[\overline{c}_0^2 + (\overline{D}/k)^2]^{-1} > 0, \qquad (2.12a)$$

$$A_w = \int_{-L/2}^{L/2} \int_0^\infty \frac{\rho}{\rho_0} \frac{\beta_e}{\overline{c}_0^2} |\phi_0|^2 \, dz' \, dy'$$
$$- \int_{-L/2}^{L/2} S^{-1} \frac{\partial\overline{u}}{\partial z} \frac{|\phi_0|^2}{\overline{c}_0^2} \, dy' \bigg|_{z=0}, \quad \text{and} \qquad (2.12b)$$

$$F(y,z) = \left(-\frac{1}{2\overline{c}_0} \frac{\partial |\phi_0|^2}{\partial z} + \frac{1}{\overline{c}_0^2} \frac{\partial \overline{u}}{\partial z} |\phi_0|^2 \right) \overline{\alpha}_y$$
$$+ \left[\overline{c}_0^2 \left| \frac{\partial}{\partial z} \left(\frac{\phi_0}{\overline{c}_0} \right) \right|^2 \frac{f_0}{N^2} \right] \overline{\alpha}_z, \qquad (2.12c)$$

where the effects of the SMD on the wave field are measured by the parameters:

$$(\overline{\alpha}_y, \overline{\alpha}_z) = \left(\overline{\Gamma} \frac{\partial \overline{\gamma}}{\partial y}, \ \overline{\Gamma} \frac{\partial \overline{\gamma}}{\partial z} \right). \qquad (2.13)$$

The growth rate equation, (2.11b), can be written as $kc_{1i}A_w = \tilde{A}_w$, which is a wave activity[2] conservation law; A_w is the domain-averaged wave activity of the

unforced (zeroth order) wave, while $\tilde{A}_w$ represents the generation or dissipation of domain-averaged wave activity due to the direct radiative effects of SMD. For the representative background flow to be examined later, $A_w > 0$.

To aid in the analysis of the propagation, growth rate, and structural characteristics of the SMD-modified waves, we supplement (2.11a) and (2.11b) with an expression for the zonally averaged generation of eddy APE by the SMD field, given by $\overline{\text{GE}} = \overline{hT}$. Using (2.6) and (2.10), and noting that the perturbation temperature is related to the geostrophic streamfunction by $T = (Hf_0 R^{-1})\partial\phi_0/\partial z$, we obtain

$$\overline{\text{GE}} = \varepsilon a_E \Lambda \left[\underbrace{-\overline{c}_0 \left(\overline{\alpha}_y + 2\frac{\partial \overline{u}}{\partial z} \frac{f_0}{N^2} \overline{\alpha}_z \right) \frac{\partial |\phi_0|^2}{\partial z}}_{\text{Baroclinic term}} + \underbrace{\left(2\overline{c}_0^2 \frac{f_0}{N^2} \overline{\alpha}_z \right) \left| \frac{\partial \phi_0}{\partial z} \right|^2}_{\text{APE term}} \right], \qquad (2.14)$$

where $a_E = \rho H f_0 R^{-1} \delta^{-1} > 0$. The baroclinic term is proportional to the zonally averaged eddy heat flux (i.e., $\overline{vT} \propto |\phi_0|_z^2 \cos\varphi$), where φ is the phase difference between the meridional wind and temperature fields. If the fields are in phase ($\varphi = 0°$), a positive heat flux ($\overline{vT} > 0$) corresponds to a local increase in the wave amplitude with height ($|\phi_0|_z^2 > 0$). If the fields are 180° out of phase, then $\overline{vT} > 0$ corresponds to $|\phi_0|_z^2 < 0$. In contrast to the baroclinic term, the APE term does not depend on the phasing of the wave field.

c. Analysis

1) GENERAL BACKGROUND FIELDS

The SMD-modified frequency, (2.11a), and growth rate, (2.11b), originate from (i) the meridional advection of zonal-mean SMD by the wave field [the term proportional to $\overline{\alpha}_y$ in (2.12c)], and (ii) the vertical advection of zonal-mean SMD by the wave field [the term proportional to $\overline{\alpha}_z$ in (2.12c)]. For both the frequency and growth rate, the $\overline{\alpha}_y$ and $\overline{\alpha}_z$ terms either augment or oppose each other depending on the combined effects of the Doppler-shifted phase speed $\overline{c}_0$, the wave structure ϕ_0, and the signs of the SMD parameters ($\overline{\alpha}_y$, $\overline{\alpha}_z$).

Equation (2.13), along with (2.7) and (2.8), shows that ($\overline{\alpha}_y$, $\overline{\alpha}_z$) are nonlinear functions of the zonal-mean SMD, as evidenced by their dependence on the product between the transmissivity parameter $\overline{\Gamma}$ and the spatial gradients of the SMD ($\overline{\gamma}_y$, $\overline{\gamma}_z$). If the SMD field is spatially uniform or locally maximized, both $\overline{\alpha}_y$ and $\overline{\alpha}_z$ vanish so that the SMD has no effect on the wave field; the SMD is simply a passive tracer that is advected by both the wave and zonal-mean background flow. The effects of the SMD on the wave field, due to either $\overline{\alpha}_y$ or $\overline{\alpha}_z$, will be maximized where the product of the zonal-mean transmissivity and spatial gradient of the SMD is maximized. For example, for a fixed transmissivity parameter $\overline{\Gamma}$, $\overline{\alpha}_y$ is maximized where the meridional SMD gradient is maximized.

Equations for the frequency, (2.11a), and growth rate, (2.11b), show that the effects of the SMD on the wave field will be most effective for A_w small, which will occur in background flows for which the Doppler-shifted phase speed is large and the background gradients in PV and surface temperature are weak.

To the extent that the small SMD-heating rate assumption used in this analytical section applies to the real atmosphere, the SMD modification to the frequency [see (2.11a)] is due solely to the dry sedimentation rate $\overline{D}$, which we have assumed in our analytical development to be independent of dust particle size. In reality, $\overline{D}$ increases as the particle size increases. Thus, the larger particles, which have greater sedimentation rates, will have their greatest effect on the wave

---

[2] Following Edmon et al. (1980), we define *wave activity* as a quantity that is quadratic in wave amplitude and that is conserved in the absence of external forcing and dissipation.

frequency during their mobilization and lofting into the atmosphere.

Equations (2.11a) and (2.11b) show that the SMD can impart to the wave field either easterly or westerly propagation, and either growth or decay depending on the signs of $\overline{\alpha}_y$ and $\overline{\alpha}_z$ and how they project onto the terms multiplying them in (2.12c). The $\overline{\alpha}_y$ term in (2.12c) can be either positive or negative depending on the sign of $\overline{\alpha}_y$ and the structures of the wave and background wind fields. The $\overline{\alpha}_z$ term in (2.12c) is always positive (negative) if $\overline{\alpha}_z > 0$ ($\overline{\alpha}_z < 0$).

We can glean additional qualitative information regarding the effects of SMD on the wave field by examining $\overline{\text{GE}}$. Inspection of (2.14) shows that the heat flux depends on the Doppler-shifted phase speed $\overline{c}_0$ and the spatial gradients of the SMD, which are proportional to $\overline{\alpha}_y$ and $\overline{\alpha}_z$, where $\overline{\alpha}_z$ is modulated by the background vertical shear and static stability. The production or destruction of $\overline{\text{GE}}$ by the baroclinic term depends on the combination of the mean wind, wave, and SMD structures. In contrast, the production or destruction of $\overline{\text{GE}}$ by the APE term depends solely on the sign of $\overline{\alpha}_z$; $\overline{\text{GE}} > 0$ (<0) for $\overline{\alpha}_z > 0$ (<0).

2) SLOWLY VARYING BACKGROUND FIELDS

We next focus on the SMD-modified complex frequency for the special case where $\overline{D} = 0$ and the background coefficients in (2.11b), (2.12), and (2.13) are assumed to be slowly varying.[3] In this case, we can assume that the background coefficients are constant to a first approximation, which permits a plane wave solution of the following form:

$$\phi_0 = \hat{\phi}_0 \exp(z/2H) \exp[i(kx + mz - \omega_0 t)] \sin ly + *,$$
$$(2.15)$$

where

$$\omega_0 = \overline{u}k - \beta_e k/K^2 \qquad (2.16)$$

is the frequency of a westward-propagating, internal Rossby wave; and

$$K^2 = k^2 + l^2 + n^2, \qquad (2.17)$$

where $l = 2\pi/L$ and $n^2 = (m^2 + 1/4H^2)$; m is the local vertical wavenumber. We note that the streamfunction (2.15) increases with altitude, though its vertical energy flux is bounded, thus satisfying the upper radiation

---

[3] *Slowly varying* is used in the context of the WKBJ formalism (e.g., Bender and Orszag 1978; Nathan and Hodyss 2010).

boundary condition that we imposed for the analytical model (see section 2a).

Insertion of (2.15) into (2.11b) and (2.12b) and (2.12c) yields, to $O(\varepsilon)$, the following expression for the SMD-modified (complex) frequency:

$$\omega = \underbrace{\left(\overline{u}k - \frac{\beta_e k}{K^2}\right)}_{\text{Frequency } \omega_0} + \underbrace{i\varepsilon a_1 \left(-\frac{\overline{\alpha}_y}{\beta_e} + 2H\frac{f_0}{N^2}\frac{n^2}{K^2}\overline{\alpha}_z\right)}_{\text{Growth rate } \omega_{1i}},$$
$$(2.18)$$

where $a_1 = \delta/2HS > 0$. If $\overline{\alpha}_y = 0$, (2.18) is, except for slight differences in notation, identical to that obtained by Ghan (1989a) for his special case where the SMD feedback rate was assumed to be much less than the internal Rossby wave frequency, an assumption that is made explicit here by $\varepsilon \ll 1$ in (2.18). As pointed out by Ghan (1989a), the growth rate is proportional to $\overline{\alpha}_z$ and is largest for waves that are relatively long and shallow, corresponding to large n^2/K^2. Although not explicitly pointed out by Ghan (1989a), the growth rate will also be larger in atmospheres that are less statically stable, corresponding to small N^2. If $\overline{\alpha}_z = 0$ and $\overline{\alpha}_y \neq 0$, then the growth rate is proportional to $\overline{\alpha}_y$; but in contrast to the $\overline{\alpha}_z$ term, the growth rate is independent of wave scale and inversely proportional to β_e. For the case where $\overline{\alpha}_y$ and $\overline{\alpha}_z$ are both nonzero, the wave exponentially amplifies provided

$$\frac{\partial \overline{\gamma}}{\partial y} < 2H\beta_e \frac{f_0}{N^2}\frac{n^2}{K^2}\frac{\partial \overline{\gamma}}{\partial z}, \qquad (2.19)$$

where we have used the definitions of the SMD parameters given by (2.13). If $\partial \overline{\gamma}/\partial y < 0$ and $\partial \overline{\gamma}/\partial z > 0$, then instability is assured; otherwise, instability will depend on the ratio of horizontal to vertical wave scales n^2/K^2, background PV gradient β_e, and static stability N^2. For example, if $\partial \overline{\gamma}/\partial y$ and $\partial \overline{\gamma}/\partial z$ are both positive and fixed, then the SMD-induced instability is squelched if n^2/K^2 or β_e are sufficiently small or if N^2 is sufficiently large.

Based on (2.15), the generation of eddy APE by the SMD field (2.14) takes the following simple form:

$$\overline{\text{GE}} \propto \varepsilon K^2 \omega_{1i} \sin^2 ly, \qquad (2.20)$$

where the SMD-induced growth rate ω_{1i} is defined in (2.18). Equation (2.20) shows that $\overline{\text{GE}}$ is proportional to the growth rate, which is modulated by the spatial scale of the wave field. If, for example, the horizontal scale of the wave field is relatively small, such that K^2 is relatively large, or if $\overline{\alpha}_y \gg \overline{\alpha}_z$, then $\overline{\text{GE}} \sim -\varepsilon K^2 \beta_e^{-1}\overline{\alpha}_y$. Thus, for $\overline{\alpha}_y < 0$, $\overline{\text{GE}}$ will be largest for shorter waves in regions where the background PV is small.

Despite the idealized nature of this subsection, which was predicated on the assumption that the background coefficients in (2.11b) were slowly varying, several of the results will carry over to the representative background flows used in the WRF-Dust model calculations to be discussed in section 3c.

3. Numerical results

a. WRF-Dust model

The subcritical destabilization of AEWs by SMD is examined using the WRF-Dust model described in Grogan et al. (2016). The model, which is an idealized version of that developed by Chen et al. (2010, 2015), couples the WRF Model to an interactive dust model. Twelve dust particle sizes, with radii ranging from 0.15 to 5 μm, each with its own continuity equation, constitute the SMD field. Following Grogan et al. (2016), each continuity equation accounts for the advection and sedimentation of SMD, where the sedimentation is represented as in Chen et al. (2008). Other SMD redistribution processes, such as subgrid cumulus and boundary layer mixing, surface emission, and wet and dry deposition, are excluded.

The daily averaged SMD heating rates, which account for shortwave heating due to SMD absorption and scattering, longwave cooling due to SMD, and the reabsorption of longwave radiation by other constituents, including water vapor, are calculated using the NASA Goddard Space Flight Center radiation (GSFC) model (Chou and Suarez 1999; Chou et al. 2001). The SMD optical properties—aerosol optical depth, single scattering albedo, and asymmetry parameter—which are required as inputs for the GSFC model, are calculated using the Optical Properties of Aerosol and Clouds (OPAC) software packages (Hess et al. 1998).

The horizontal model domain is a global channel projected onto a cylindrical–equidistant grid that extends from 10°S to 40°N, with a horizontal resolution of 0.5°. To satisfy the Courant–Friedrichs–Lewy (CFL) condition, a 3-min time step is used. The vertical domain is divided into 50 terrain-following levels; there is no bottom topography, and the pressure at the model top is 100 hPa. The boundary conditions are periodic in the east–west direction, symmetric at the north and south channel walls, and free slip at the top and bottom boundaries. A 30-min hyper diffusion is imposed on the wind fields.

b. Background state and initial conditions

The theoretical framework developed in section 2 is valid for any subcritical, zonal-mean background state. How that background state is obtained is

therefore irrelevant to the interpretation of the analytical expressions for the SMD-modified growth rate and frequency. Our approach to constructing a background state that is subcritical with respect to barotropic and baroclinic instability proceeds as follows. First, we initialize the WRF-Dust model using the supercritical, zonal-mean background wind (AEJ) used by Grogan et al. (2016, their Fig. 1). As in many previous studies (e.g., Simmons 1977; Thorncroft and Hoskins 1994), the Grogan et al. (2016) zonal-mean background wind is chosen to be analytical in form and is consistent with observations. Using this initial (supercritical) background wind, we then follow Grogan et al. (2017) and superimpose a synoptic-scale perturbation in the horizontal wind field. The perturbation is chosen constant in the latitude–height plane with an amplitude of 1.0 m s^{-1} and zonal wavenumber k = 12 (wavelength of $\sim$3300 km). This wavenumber corresponds to the fastest-growing wave in the model and is consistent with the zonal scales of observed AEWs found by Kiladis et al. (2006), among others. Given the initial perturbation, we then integrate the model forward in time until the nonlinear wave fluxes stabilize the AEJ. The stabilization was confirmed by ensuring that the Charney and Stern (1962) necessary condition for instability was not satisfied. The stabilization of the AEJ occurs after $\sim$10 model days, at which time the zonal-mean wind and potential temperature fields constitute our new subcritical background state. Such a background state, however, will generally not satisfy the WRF-Dust model equations. To resolve this problem, we follow the methodology of Hall et al. (2006) and Grogan et al. (2016) and introduce, in the wave-free state, an external forcing such that each of the background fields satisfy a prognostic equation of the form $d\mathbf{X}/dt = \mathbf{F}_0 + \mathbf{F}_B$. The vectors $\mathbf{X}$, $\mathbf{F}_0$, and $\mathbf{F}_B$ represent, respectively, the background variables, the original forcings of the variables, and an imposed external forcing that ensures a steady, zonal-mean background state.

Figure 1 shows the subcritical, zonal-mean wind and potential temperature distributions that will constitute our background state, along with the corresponding quasigeostrophic PV distribution β_e, which we note does not reverse sign in the latitude–height plane. The AEJ axis is centered at $\sim$11°N and has a peak easterly wind speed of $\sim$8 m s^{-1} at $\sim$630 hPa. These AEJ characteristics are consistent with Afiesimama (2007), who used NCEP–NCAR reanalysis data spanning 1971–2000 to characterize the annual variability of the zonal wind over West Africa. He found that, for July–August, the location of the mean jet core varies between about
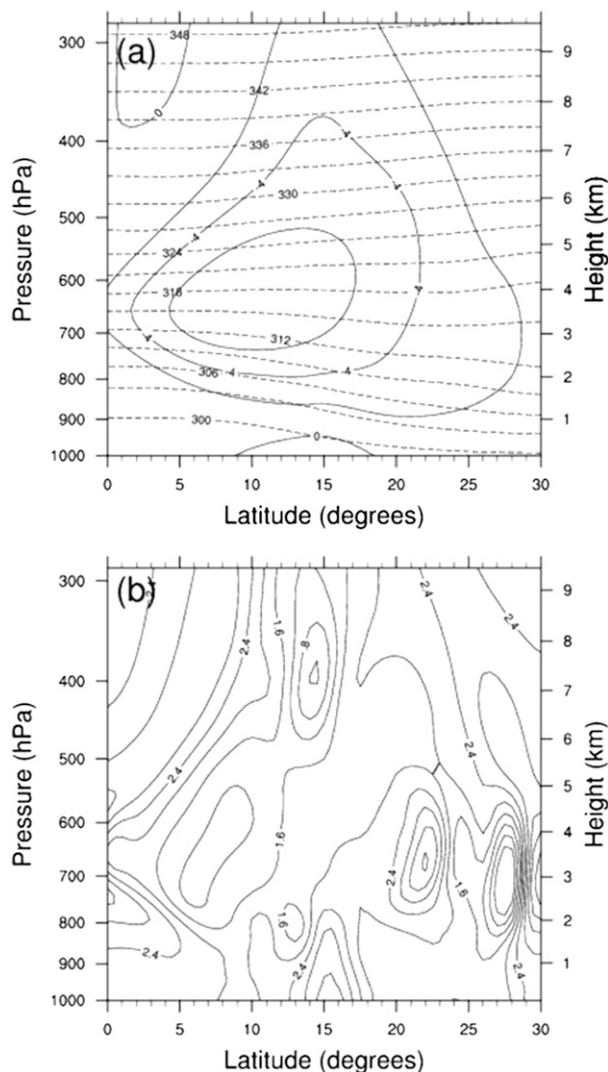
FIG. 1. (a) Background distributions of the zonal-mean wind (solid; contour interval: $2 \, \text{m s}^{-1}$) and zonal-mean potential temperature (dashed; contour interval: 3 K). (b) Quasigeostrophic PV gradient from (2.4) (contour interval: $0.4 \times 10^{-11} \, \text{m}^{-1} \, \text{s}^{-1}$) corresponding to the zonal-mean flow shown in (a).

$10°$ and $14°$N, while the peak easterly wind speed is about $\sim 8 \, \text{m s}^{-1}$ at $\sim 600 \, \text{hPa}$.

The subcritical background flow shown in Fig. 1 will be used for all of the numerical experiments presented below, regardless of whether the experiments include SMD. As discussed by Grogan et al. (2016), the advantage of fixing the background flow is that any SMD-induced instabilities that arise are due solely to the interactions involving the wave fields in wind, temperature, and SMD and not to changes in the background flow. The fixed-background-flow approach, as discussed in Cho and Jenkins (1987), is valid, provided the ratio of diabatic-induced divergences to the relative vorticity,

denoted by $\hat{\varepsilon}$, is weak, a condition that ensures the diabatic forcing has a relatively small effect on the background flow. For the representative SMD distributions that we will discuss next, $\hat{\varepsilon} \approx 0.1$.

Figure 2 shows the spatial distributions of the background SMD mass mixing ratio $\overline{\gamma}$ and the corresponding SMD parameters $\overline{\alpha}_y$ and $\overline{\alpha}_z$, defined by (2.13). The SMD distribution shown in Fig. 2a, which is based on the analytical representation given by Grogan et al. (2016), is qualitatively consistent with summertime observations over the Sahara (Kaufman et al. 2005). The distribution is centered at $20°$N, which resides within the main latitude belt for SMD emission (Engelstaedter and Washington 2007). The SMD is normally distributed in latitude with a half-width of $2.5°$; and it is well mixed up to $\sim 700 \, \text{hPa}$, which is the approximate height of the convective boundary layer over the Sahara (Cuesta et al. 2009). Above $\sim 700 \, \text{hPa}$, the SMD monotonically decreases, reaching zero by $\sim 500 \, \text{hPa}$. In Grogan et al. (2016), each of the 12 SMD particle sizes were assumed to have the same mixing ratio. Here we choose a more realistic lognormal distribution for the mixing ratios, which we base on observed emissions over the Sahara (Kok 2011). To obtain a *maximum* shortwave ($0.5 \, \mu\text{m}$) AOD of $\overline{\tau} = 1.0$,[4] a moderate value that is consistent with observations (Kaufman et al. 2005) and other modeling studies (Ma et al. 2012), the SMD mixing ratios have been scaled accordingly. The maximum total SMD mass mixing ratio from the 12 SMD particles is $\sim 800 \, \mu\text{g kg}^{-1}$.

Figures 2b and 2c show the distributions of $\overline{\alpha}_y$ and $\overline{\alpha}_z$, which were shown in section 2 to play a critical role in the SMD-modified frequency and growth rate. The SMD parameter $\overline{\alpha}_y$ has two lobes that straddle the SMD maximum; the positive (negative) lobe is centered at $\sim 18°$N ($22°$N), which approximately coincides with the location where the magnitude of the SMD gradient $|\overline{\gamma}_y|$ is largest, consistent with the discussion in section 2c. The SMD parameter $\overline{\alpha}_z$ is negative, and its magnitude is largest at $20°$N, $650 \, \text{hPa}$.

To numerically calculate the growth rate, phase speed, and structure of the AEWs, we use an initial value approach (Simmons 1977; Thorncroft and Hoskins 1994; Grogan et al. 2016). Given the subcritical background state shown in Fig. 1 and a specified zonal wavenumber, we initialized the WRF-dust model with the latitude–height wave structure that was obtained at the same time the subcritical AEJ was obtained. An initial amplitude

---

[4] The maximum AOD of $\overline{\tau} = 1.0$ occurs at the center of the Gaussian plume shown in Fig. 2 and decreases to 0.5 at $\sim 17°$ and $\sim 23°$N.
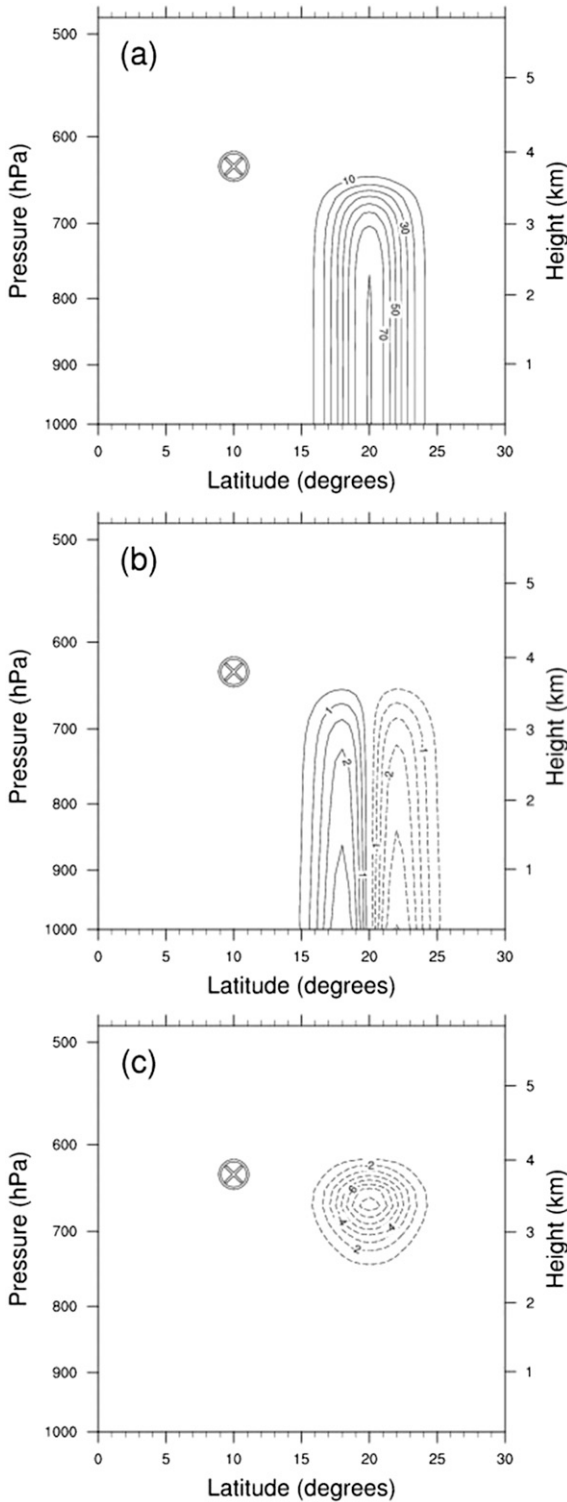
FIG. 2. (a) Background SMD mass mixing ratio $\overline{\gamma}$ (contour interval: $\mu g \, kg^{-1} \times 10$), and SMD parameters: (b) $\overline{\alpha}_y$ (contour interval: $0.5 \, m^2 \, s^{-3}$) and (c) $\overline{\alpha}_z$ (contour interval: $1.0 \, m^2 \, s^{-3}$). The symbol $\otimes$ denotes the location of the background jet maximum (see Fig. 1a). Solid contours denote positive values.
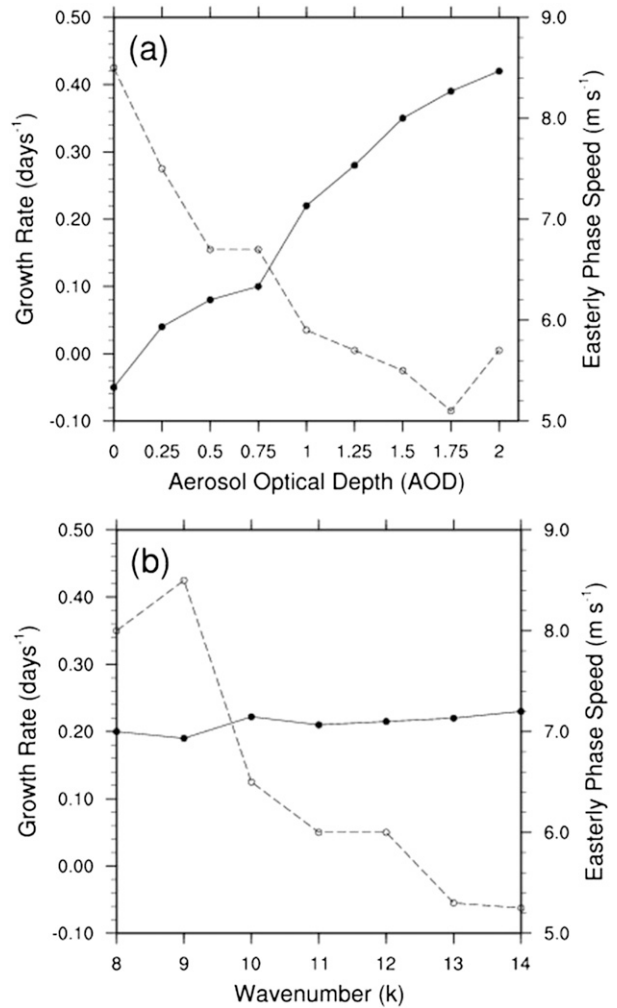

FIG. 3. Growth rate (solid) and phase speed (dashed) as a function of (a) maximum AOD and (b) zonal wavenumber k ($\overline{\tau} = 1$).

of $10^{-3} \, m \, s^{-1}$ was chosen for the horizontal wind. The growth rate was determined by integrating the model forward in time until the domain-averaged total eddy energy achieved exponential growth to an accuracy of 10^{-3} for at least 24 h. The phase speed was determined by tracking the wave for one model day after it achieved exponential growth. To ensure that the simulation remained within the linear regime, we calculated the ratio of the disturbance wind speed to the maximum background wind speed and required that it remain small (<0.05) throughout the integration. Other initial wave amplitudes and structures were tested and, as expected, all produced the same results.

c. Results

Figure 3a shows the phase speeds and growth rates for maximum AODs ranging from $\overline{\tau} = 0$ (no dust) to $\overline{\tau} = 2$.
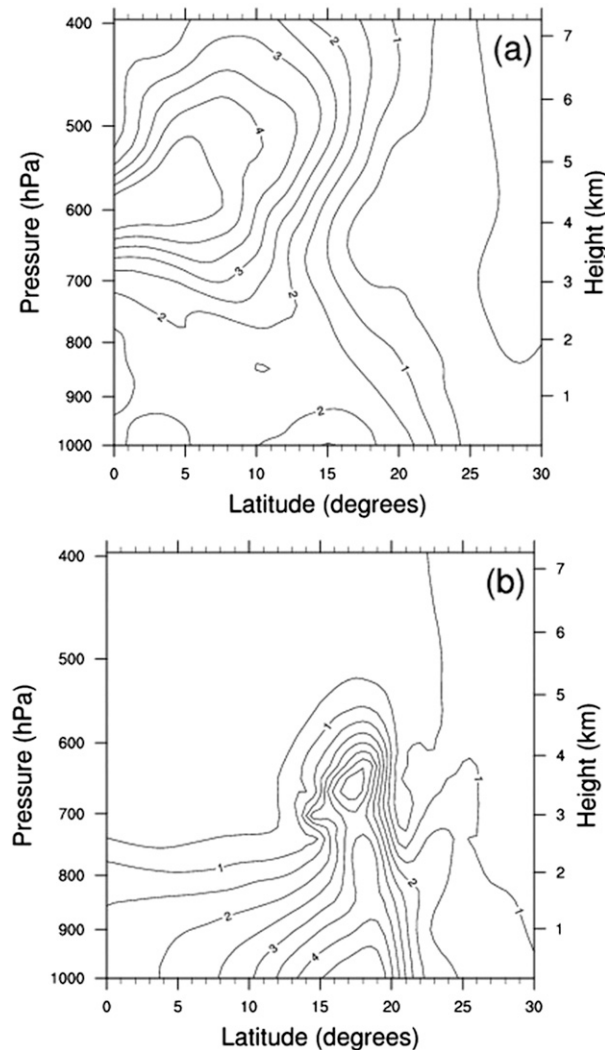
FIG. 4. Amplitude modulus of the meridional wind ($m\,s^{-1}$) obtained from the WRF-Dust model: (a) without SMD and (b) with SMD. In the context of the theoretical framework presented in section 2, the structure in (a) is the numerically determined counterpart to the analytically determined meridional wind $|\partial\phi_0/\partial x|$, whereas in (b) it is the counterpart to $|\partial\phi_0/\partial x| + \varepsilon|\partial\phi_1/\partial x|$. The wave field has been scaled to produce a maximum meridional velocity of $5\,m\,s^{-1}$.

Consider first the phase speeds. The easterly phase speed in the SMD-free case ($\overline{\tau} = 0$) is always greater than the easterly phase speed in the SMD-modified case ($\overline{\tau} \neq 0$). For example, for $\overline{\tau} = 1$, the easterly phase speed is $\sim 5.9\,m\,s^{-1}$, which is $\sim 30\%$ slower than the SMD-free case. This means that, for an SMD-induced instability that originates near the Bodélé depression in Chad, a major SMD source region (Engelstaedter and Washington 2007), the wave will arrive at the West African coast ~ 2.4 days later than in the SMD-free case.

For the growth rates, Fig. 3a shows that, in the absence of SMD ($\overline{\tau} = 0$), the growth rate is $-0.04\,day^{-1}$, which corresponds to slow decay of the wave, a consequence of the mechanical diffusion in the WRF-Dust model. As $\overline{\tau}$ increases, the growth rate also increases. The growth rates for $\overline{\tau} = 1$ and $\overline{\tau} = 2.0$ are, respectively, 0.22 and $0.42\,day^{-1}$. These SMD-induced growth rates are comparable to, and even exceed, those obtained in idealized models in which the zonally averaged background state is supercritical and the effects of SMD are excluded [e.g., Table 1 in Hall et al. (2006)].

Figure 3b shows, for $\overline{\tau} = 1$, the variations in easterly phase speed and growth rate for zonal wavenumbers $k = 8$–14. The maximum easterly phase speed of $\sim 8.45\,m\,s^{-1}$ occurs for $k = 9$ and monotonically decreases thereafter. Over the range $k = 8$–14, the phase speed varies by a factor of 5. The growth rate, however, is relatively insensitive to changes in k, averaging $\sim 0.20\,day^{-1}$ and varying by only $\sim 10\%$.

The physics underlying the SMD-induced changes to the growth rate and frequency described above can be explained using the theoretical framework developed in section 2. To do so, we first note that the WRF-Dust model calculations show that the $\overline{\alpha}_y$ terms in (2.11a) and (2.11b) dominate over the $\overline{\alpha}_z$ terms (growth rates change by $<10\%$ if $\overline{\alpha}_z$ is neglected). We therefore set $\overline{\alpha}_z = 0$, which allows us to simplify (2.11a) and (2.11b); we begin with the growth rate:

$$kc_{1i} \approx \frac{1}{A_w}\int_{-L/2}^{L/2}\int_0^\infty \frac{\rho}{\rho_0}\Lambda\underbrace{\left(-\frac{1}{2}\frac{\partial|\phi_0|^2}{\partial z} + \frac{1}{\overline{c}_0}\frac{\partial\overline{u}}{\partial z}|\phi_0|^2\right)}_{G(y,z)}\overline{\alpha}_y\,dz'dy',$$

(3.1)

where $\Lambda > 0$ is defined by (2.12a) and $G(x, y)$ may be positive or negative depending on the disturbance and background wind distributions. Equation (3.1) shows that a positive growth rate is determined by where $G\overline{\alpha}_y$ is large and positive in the latitude–height plane. Evaluation of G requires knowledge of the SMD-free wave structure $|\phi_0|$, the Doppler-shifted phase speed $\overline{c}_0$, and the zonal-mean wind distribution $\overline{u}$.

Consider first the analytical representation of the SMD-free wave structure $|\phi_0|$. In the quasigeostrophic formalism, the meridional wind is given by $v \propto \partial\phi/\partial x$ (Pedlosky 1987). It follows from (2.9) that $|v_0| \propto k|\phi_0|$, which is the analytical counterpart to the numerically determined meridional wind structure shown in Fig. 4a. With this information and the distribution of $\overline{c}_0$ shown in Fig. 5, we can now interpret G in (3.1).

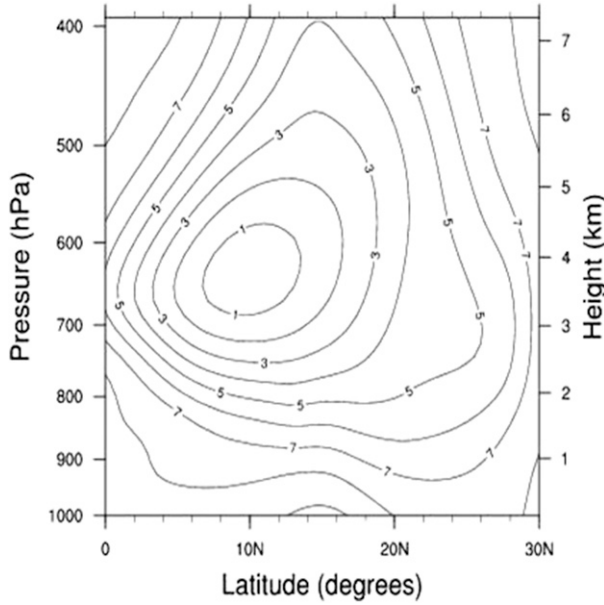Calculations of the linear stability properties from the WRF-Dust model show that the first term in G

FIG. 5. Doppler-shifted phase speed $\overline{c}_0 = \overline{u} - c_0$ (m s^{-1}).

FIG. 6. Generation of eddy APE by the SMD field $\overline{\text{GE}}$ in the WRF-Dust model (m^2 s^{-3} $\times$ 10^{-5}). The symbol $\otimes$ denotes the location of the background jet maximum (see Fig. 1a). Solid contours denote positive values.

dominates over the second, except where $\overline{c}_0 \to 0$, which occurs near the jet core, a region well removed from the SMD plume. Figure 4a indicates that, below about 700 hPa, $\partial|\phi_0|^2/\partial z$, which is negative between about 17° and 23°N, is larger on the south side of the plume where $\overline{\alpha}_y > 0$ and maximized. Thus, the integrand in (3.1) is most heavily weighted in the region centered near 18°N (i.e., where $G\overline{\alpha}_y > 0$). Consequently, the growth rate is positive.

Based on qualitative knowledge of the wave and SMD structures, we have deduced that the radiative–dynamical feedbacks operating in the region centered around 18°N carry the greatest weight in the domain and therefore would result in wave growth, in agreement with the WRF Model results. Examination of the generation of APE by the SMD field ($\overline{\text{GE}}$) further confirms the importance of the region near 18°N to the growth of the wave. Figure 6 shows that $\overline{\text{GE}} > 0$ and is a maximum near 18°N, 700 hPa. This is consistent with the prediction of the theoretically derived expression for $\overline{\text{GE}}$, which, from (2.14), can be approximated as
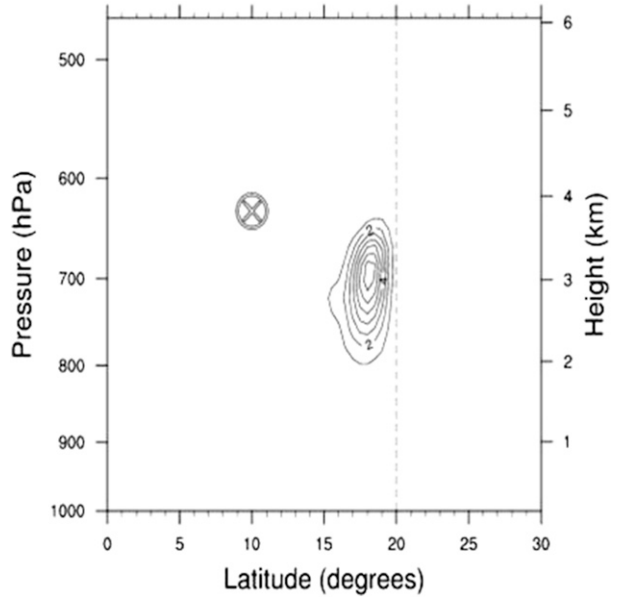
where, for simplicity, we have ignored sedimentation ($\overline{D} = 0$) and again used $\overline{\alpha}_y \gg \overline{\alpha}_z$ based on the WRF-Dust model calculations. Figures 2b, 4a, and 5 show, respectively, that $\overline{\alpha}_y > 0$, $\partial|\phi_0|^2/\partial z < 0$, and $\overline{c}_0 > 0$ near 18°N so that $\overline{\text{GE}} > 0$ is large there and negligible elsewhere. The fact that the region $\overline{\text{GE}} > 0$ dominates over that for $\overline{\text{GE}} < 0$ in Fig. 6 is due to $\overline{c}_0 > 0$ and $\partial|\phi_0|^2/\partial z < 0$ both having greater magnitudes near 18°N, 700 hPa rather than near 22°N, 700 hPa.

The SMD-induced changes to the phase speed shown in Fig. 3 can be explained by assuming that $\overline{\alpha}_y \gg \overline{\alpha}_z$, the same assumption that we used to explain the SMD-induced growth rate. It follows that (2.11a) can be written as

$$\overline{\text{GE}} \propto -\frac{\overline{\alpha}_y}{\overline{c}_0} \frac{\partial|\phi_0|^2}{\partial z}, \qquad (3.2)$$

$$kc_{1r} \approx \frac{1}{A_w} \int_{-L/2}^{L/2} \int_0^\infty \frac{\overline{D}}{k\overline{c}_0} \frac{\rho}{\rho_0} \Lambda \underbrace{\left(-\frac{1}{2} \frac{\partial|\varphi_0|^2}{\partial z} + \frac{1}{\overline{c}_0} \frac{\partial\overline{u}}{\partial z}|\varphi_0|^2 \right)}_{G(x,y)} \overline{\alpha}_y \, dz' \, dy', \qquad (3.3)$$

which differs from (3.1) by the factor $\overline{D}/k\overline{c}_0$. Because we have established that the integrand is dominated by $G\overline{\alpha}_y > 0$, (3.3) shows that the SMD-induced phase speed

c_{1r} is negative since the sedimentation rate $\overline{D}$ is negative. Consequently, the SMD increases the easterly phase speed of the wave field. But this contradicts the
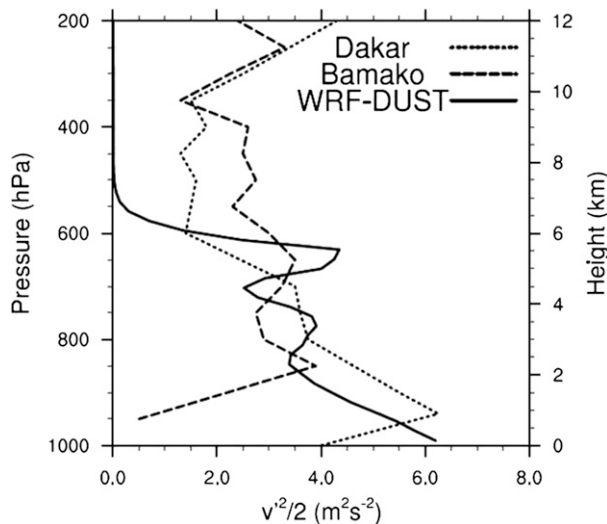
FIG. 7. AEW vertical structure (measured by meridional wind variance): WRF-Dust model (solid; 18°N); Bamako (dashed; 12.5°N, 8.0°W); and Dakar (dotted; 14.7°N, 17.5°W). The WRF-Dust model wind variance is zonally averaged and based on a maximum meridional velocity of $5\,\mathrm{m\,s^{-1}}$. The structures for Bamako and Dakar, averaged for June 1995, are from Pytharoulis and Thorncroft (1999).

numerical results shown in Fig. 3, which show that the SMD decreases the easterly phase speed. This apparent contradiction is resolved by noting the following. In the absence of SMD, the theoretical framework yields, for the SMD-free case, a real easterly phase speed c_0; this reflects our initial assumption that the wave is neutral to zeroth order. In the WRF-Dust model, however, the SMD-free case yields a damped wave, a consequence of the mechanical diffusion in the model. To align the theoretical framework with the WRF-Dust model, we assume that to zeroth order the wave can either grow or decay such that $c_0 \to c_{0r} + ic_{0i}$, which allows us to write $\overline{c}_0 \to \overline{u} - c_{0r}$ and $\overline{D}k^{-1} \to \tilde{D}k^{-1} = \overline{D}k^{-1} - c_{0i}$ in (3.3). If $c_{0i} < 0$ and is sufficiently large, then $\tilde{D} > 0$ so that $c_{1r} > 0$. In this case, given that to $O(\varepsilon)$ the phase speed is $c_{0r} + \varepsilon c_{1r}$, where $c_{0r} < 0$ and $c_{1r} > 0$, the SMD decreases the easterly phase speed, in agreement with the WRF Model results. If $c_{0i} > 0$, then $c_{1r} < 0$ so that the SMD increases the easterly phase speed, in agreement with the supercritical results obtained by Grogan et al. (2016).

The SMD-free wave structure shown in Fig. 4a was used to explain the physics of the SMD-modified growth rate and frequency obtained from the WRF-Dust model. The SMD-modified wave structure is shown in Fig. 4b. Comparison of Figs. 4a and 4b shows that the SMD produces a more highly structured wave (i.e., a wave with multiple extrema in the vertical) and

increases its amplitude by almost a factor of 5 near 18°N, 750 hPa, the same region where $\overline{GE}$ is maximized (see Fig. 6). Moreover, the maxima in the SMD-modified AEW structure coincide with the observed north track of the AEWs, located between ~18° and 25°N (Reed et al. 1988), the same region where the major SMD sources are located (Engelstaedter and Washington 2007).

Similar to the AEW structure shown in Fig. 4b, observations over North Africa also show highly structured AEWs (Fig. 7). For example, Pytharoulis and Thorncroft (1999) used reanalysis data to calculate the AEW vertical structure at Bamako (dashed; 12.5°N, 8.0°W) and Dakar (dotted; 14.7°N, 17.5°W) for each of 4 months spanning June–September 1995 and for the average of the 4 months. They find that the vertical structure is highly variable in height and time. For instance, over the 4 months, the structure at a given level is shown to vary by as much as a factor of 6.

In light of the results obtained by Pytharoulis and Thorncroft (1999), we show in Fig. 7 the vertical variations in the meridional wind variance at 18°N obtained from the WRF-Dust model, together with the variance at Bamako (dashed) and Dakar (dotted) averaged for June 1995. All three cases are characterized by considerable vertical variability. The three cases differ, however, in several ways, including in the number of local extrema and in the vertical extent. In addition, the vertical structure from the WRF-Dust model decreases with height near the lower boundary, whereas it increases with height at both Bamako and Dakar. The simplified boundary layer physics in our idealized WRF-Dust model—which, recall, excludes boundary layer mixing, surface emission, and wet and dry deposition—may account for the different wave structure in the lower atmosphere. Also, it is unclear to what extent the structures over Bamako and Dakar are themselves influenced by the SMD. The important point here is that the large increases in amplitude and the highly structured nature of the wave shown in Fig. 4b are due solely to the radiative–dynamical feedbacks involving the SMD and not to the background wind and temperature structures.

4. Conclusions and discussion

a. Conclusions

Studies of AEWs have occupied more than four decades of research, evidence of their importance to the meteorology over North Africa and the eastern Atlantic Ocean. A large body of that research attributes the

origin of the AEWs to the combined barotropic–baroclinic instability of the AEJ. Such supercritical AEJs, however, only occur episodically. Indeed, observations show that the AEJ shows considerable intraseasonal variability (Afiesimama 2007; Leroux and Hall 2009). It is therefore likely that the AEJ will be subcritical with respect to synoptic-scale waves at various times throughout the summer. During such times, we have shown theoretically and numerically that it is still possible to generate, via radiative–dynamical feedbacks involving SMD aerosols, disturbances with AEW-like characteristics.

To explain the radiative–dynamical feedbacks that govern the SMD-induced instabilities, we have developed a theoretical framework based on coupled equations for quasigeostrophic PV, temperature, and SMD mixing ratio. The theoretical framework, which is sufficiently general that it can be applied to any subcritical, but otherwise arbitrary, zonal-mean background state, yields, via a perturbation analysis, analytical expressions for the SMD-induced growth rate and frequency of AEW-like waves. The expressions are functions of the domain-averaged wave activity, which is modulated by the Doppler-shifted phase speed and the background gradients in PV and SMD. Depending on how these three flow features combine with the wave structure, the SMD may be stabilizing or destabilizing.

Although the theoretical framework was built around a quasigeostrophic atmosphere, with several simplifying assumptions, including a small SMD heating rate due solely to shortwave absorption, it has proven robust; it explains the linear stability results that we have obtained using an idealized version of the WRF-Dust model developed by Chen et al. (2015). The model results show, for example, that, for a subcritical AEJ and background SMD distribution that are consistent with observations, the SMD destabilizes the AEWs and slows their westward propagation, consistent with the prediction of the theoretical framework. The SMD-induced instabilities have growth rates that are commensurate with, and can sometimes exceed, those obtained in previous idealized SMD-free studies in which the AEWs grow on zonal-mean, supercritical AEJs. Moreover, we find that the slowing of the westward propagation of the instabilities is such that an SMD-induced AEW originating near the Bodélé depression in Chad would arrive at the West African coast more than 2 days later than in the SMD-free case. This means that the weather forecasts for North Africa will need to accurately account for the feedbacks between the SMD and the circulation in order to accurately account for the strength and timing of AEW activity.

b. Discussion

To the extent that the results obtained in this study carry over to zonally varying background states, they may be particularly relevant to results obtained by Hall et al. (2006, p. 2243), who showed that for a realistic zonally varying AEJ, "a reasonable amount of low-level damping" can neutralize synoptic-scale disturbances. They conclude that "barotropic–baroclinic instability alone cannot explain the initiation and intermittence of AEWs, and a finite amplitude initial perturbation is required" (Hall et al. 2006, p. 2231). In a subsequent paper, Thorncroft et al. (2008, p. 3596) show, using a primitive equation model, that "AEWs can be triggered by finite-amplitude transient and localized latent heating on a zonally varying background state that is linearly stable." Based on our results, it is conceivable that, in a realistic zonally varying AEJ, the destabilizing effects of SMD may alone offset the neutralization of the AEWs produced by realistic low-level damping, leading to the development of otherwise neutral or even damped AEWs.

In addition to possibly offsetting the neutralization of AEWs by low-level damping, the subcritical destabilization of AEWs by SMD shown in this study may also contribute to the intermittency of AEWs. For example, Leroux and Hall (2009) have shown that, even if AEWs are triggered by convection, as suggested by Thorncroft et al. (2008), the AEJ is still important to determining the propagation and growth of the AEWs. Leroux and Hall (2009) show that, given the same convective trigger, stronger (weaker) AEWs tend to develop in zonally varying AEJs with stronger (weaker) PV gradient reversals. We have shown that even when the PV gradient does not change sign (i.e., when the zonally mean AEJ is subcritical with respect to the barotropic–baroclinic instability threshold), the SMD can still produce AEW-like disturbances.

Combining our result with that of Leroux and Hall (2009) raises the following question: Is it possible for convective activity to trigger strong AEWs even when the AEJ does not possess a PV gradient reversal? This may indeed be the case given that we have shown that the radiative–dynamical feedbacks involving SMD can generate eddy APE and thus AEW-like disturbances, even in an environment where the background PV gradient does not reverse sign. Of course, whether this is the case will require accounting for the feedbacks involving the SMD, AEJ, AEWs, and convective

activity. This is a complicated problem, which, in its entirety, must account for the radiative and cloud microphysical effects of the SMD on the AEJ–AEW–convective system.

Leroux et al. (2011) have shown that convective activity is not the only mechanism that can affect the intermittency of AEWs. They show, using a dry general circulation model, that the model-generated AEWs can be triggered by precursor disturbances originating from the North Atlantic storm track. As the disturbances propagate eastward, they eventually reach the western Mediterranean where they turn southward toward Lake Chad in North Africa. It is interesting to note that Lake Chad is on the southern boundary of the Bodélé depression, a major dust source region (Engelstaedter and Washington 2007). One could therefore envision the following scenario. As the precursor disturbances move into North Africa, they mobilize the SMD to form a plume that changes the thermal structure of the atmosphere, affecting not only the precursor disturbances themselves through SMD-dynamical feedbacks, but also the structure of the AEJ and the triggering of the AEWs.

In light of our study and those of Leroux and Hall (2009) and Leroux et al. (2011), further work is needed regarding the combined effects of the SMD and the nature of the initial perturbations, whether generated by local convection or by precursor disturbances originating along the North Atlantic storm track. As a first step in obtaining a more complete picture of the effects of SMD on the genesis and intermittency of AEWs, the present study needs to be extended to zonally varying flow. This is important because the major SMD source regions are strongly zonally varying, as are the AEJ and the initial triggering perturbations. Moreover, to obtain a more complete picture of the quantitative aspects of the SMD-induced instabilities, sensitivity studies are needed. For example, for what combination of initial perturbations, background flow structure, and SMD characteristics—distribution, location, and amount—are the growth rates of the AEWs optimized. And what are the corresponding energetics and phase relationships of the eddy fields in wind, temperature, and SMD? In addition, it is of interest to examine how the SMD-induced instabilities found in this study, which were based on an SMD distribution consistent with the region over the Sahara, change over the eastern Atlantic, where the SMD and higher humidity will together produce a different radiative heating distribution than over the Sahara, as shown by Carlson and Benjamin (1980). The theoretical framework developed in this study

will aid in answering these unresolved and important issues.

APPENDIX A

SMD Heating Rate in the Quasigeostrophic Model

For the analytical analysis presented in section 2, we assume a gray, plane-parallel atmosphere without scattering. Under these assumptions, the diabatic heating rate per unit mass as a result of a shortwave absorber, such as dust, can be written as (Liou 2002)

$$
\begin{aligned}
\dot{H} = -\frac{\partial F_d}{\partial z} &= \mu S_0 \frac{\partial}{\partial z} \exp\left(-\frac{1}{\mu} \int_z^\infty \sigma_a \rho \gamma_T \, dz'\right) \\
&= S_0 \sigma_a \rho \gamma_T \exp(-\tau_T),
\end{aligned} \tag{A.1}
$$

where F_d is the radiant flux density, μ is the cosine of the solar zenith angle, S_0 is the solar constant, σ_a is the specific absorption coefficient, $\gamma_T = \overline{\gamma}(y, z) + \gamma(x, y, z, t)$ is the total SMD mass mixing ratio, and $\tau_T = \overline{\tau}(y, z) + \tau(x, y, z, t)$ is the total AOD, given by

$$
\tau_T = \frac{1}{\mu} \int_z^\infty \sigma_a \rho \gamma_T \, dz'. \tag{A.2}
$$

The remaining symbols are defined in Table 1. Insertion of γ_T and τ_T into (A.1) and linearizing yields the following expression for the perturbation SMD heating rate:

$$
\begin{aligned}
\dot{h} &= S_0 \sigma_a \rho (\gamma \exp^{-\overline{\tau}} + \overline{\gamma} \exp^{-\tau}) \\
&= S_0 \sigma_a \rho (\gamma \overline{T}_r + \overline{\gamma} T_r).
\end{aligned} \tag{A.3}
$$

The first term in the parentheses is the contribution to the local SMD heating rate, which involves the product of the perturbation SMD γ and the mean transmissivity $\overline{T}_r$. The second term, referred to as the shielding effect, represents the contribution to the SMD heating rate due to variations in column SMD above a given level.

Previous studies have shown that, for a trace absorber, the shielding term, which involves the product between the mean SMD $\overline{\gamma}$ and the perturbation transmissivity T_r can be neglected if the absorber perturbations are relatively shallow (Ghan 1989b; Nathan 1989; Nathan and Li 1991; Echols and Nathan 1996; Grogan et al. 2012). Such is the case for North Africa, where the SMD is usually confined below ~500 hPa (Grogan et al. 2016). For this reason, and because the analytical analysis only seeks to provide qualitative relationships rather than quantitative measures of the dust-modified instability of AEWs, the shielding effect is neglected. With this additional assumption, (A.3) becomes $\dot{h} = \overline{\Gamma}\gamma$, where the coefficient $\overline{\Gamma}(y, z; \overline{\gamma})$ is defined by (2.7).

APPENDIX B

Dust-Modified Frequency and Growth Rate

Expressions for the SMD-modified frequency and growth rate are obtained by first defining the nth-order perturbation quasigeostrophic PV as

$$q_n = -k^2 \phi_n + \frac{\partial^2 \phi_n}{\partial y^2} + \frac{1}{\rho} \frac{\partial}{\partial z} \left(\frac{\rho}{S} \frac{\partial \phi_n}{\partial z} \right). \quad (B.1)$$

Insertion of (2.9) into (2.1)–(2.3) then yields to zeroth order

$$(\overline{u} - c_0) q_0 + \beta_e \phi_0 = 0, \quad (B.2)$$

$$(\overline{u} - c_0) \gamma_0 + \phi_0 \frac{\partial \overline{\gamma}}{\partial y} - ik^{-1} w_0 \frac{\partial \overline{\gamma}}{\partial z} = -ik^{-1} \overline{D} \gamma_0, \quad (B.3)$$

$$(\overline{u} - c_0) \frac{\partial \phi_0}{\partial z} - \phi_0 \frac{\partial \overline{u}}{\partial z} - ik^{-1} \frac{N^2}{f_0} w_0 = 0, \quad \text{and}$$

$$(\overline{u} - c_0) \frac{\partial \phi_0}{\partial z} - \phi_0 \frac{\partial \overline{u}}{\partial z} = 0 \quad \text{for} \quad z = 0. \quad (B.4)$$

For subcritical background states subject to the sidewall and radiation boundary conditions described in section 2a, (B.1) yields an adiabatic free-wave solution with real amplitude $\phi_0(y, z)$ and real frequency ω_0. Combining (B.2) and (B.3) yields the (complex) SMD amplitude:

$$\gamma_0 = [(\overline{u} - c_0) + ik^{-1}\overline{D}]^{-1}$$
$$\times \left\{ -\phi_0 \frac{\partial \overline{\gamma}}{\partial y} + \frac{f_0}{N^2} \left[(\overline{u} - c_0) \frac{\partial \phi_0}{\partial z} - \frac{\partial \overline{u}}{\partial z} \phi_0 \right] \frac{\partial \overline{\gamma}}{\partial z} \right\}. \quad (B.5)$$

The $O(\varepsilon)$ balance is

$$(\overline{u} - c_0) q_1 + \beta_e \phi_1 = -ik^{-1} \frac{\delta}{\rho} \frac{\partial}{\partial z} \left(\frac{\rho}{S} \overline{\Gamma} \gamma_0 \right) + c_1 q_0, \quad (B.6)$$

$$(\overline{u} - c_0) \gamma_1 + \phi_1 \frac{\partial \overline{\gamma}}{\partial y} - ik^{-1} w_1 \frac{\partial \overline{\gamma}}{\partial z} + ik^{-1} \overline{D} \gamma_1 = c_1 \gamma_0, \quad (B.7)$$

$$(\overline{u} - c_0) \frac{\partial \phi_1}{\partial z} - \phi_1 \frac{\partial \overline{u}}{\partial z} - ik^{-1} \frac{N^2}{f_0} w_1 = -i \frac{\kappa}{H} k^{-1} \overline{\Gamma} \gamma_0 + c_1 \frac{\partial \phi_0}{\partial z}, \quad (B.8)$$

and

$$(\overline{u} - c_0) \frac{\partial \phi_1}{\partial z} - \phi_1 \frac{\partial \overline{u}}{\partial z} = -i \frac{\kappa}{H} k^{-1} \overline{\Gamma} \gamma_0 + c_1 \frac{\partial \phi_0}{\partial z} \quad \text{for} \quad z = 0. \quad (B.9)$$

Equations (B.6)–(B.9) contain forcing terms on the right-hand side that project onto the linear operator. If the terms are not removed, the expansions for ϕ, γ, and w given by (2.9) would be invalid. Thus, to ensure the validity of (2.9), we apply a solvability condition that will yield the sought after expression for the dust-modified (complex) frequency kc_1. The solvability condition requires multiplying (B.6) by $(\overline{u} - c_0)^{-1} \rho S \phi_0^*$, integrating over the domain, and applying the upper and lower boundary conditions. The result is

$$kc_1 = i \frac{\delta}{A_w} \int_{-L/2}^{L/2} \int_0^\infty \frac{\rho}{\rho_0} \frac{\partial P_0}{\partial z} \frac{\overline{\Gamma}}{S} \gamma_0 \, dz' \, dy', \quad (B.10)$$

where

$$A_w = \int_{-L/2}^{L/2} \int_0^\infty \frac{\rho}{\rho_0} \beta_e |P_0|^2 \, dz' \, dy' - \int_{-L/2}^{L/2} \frac{1}{S} \frac{\partial \overline{u}}{\partial z} |P_0|^2 \bigg|_{z=0}, \quad (B.11)$$

and

$$P_{0z} = \frac{\partial P_0}{\partial z} = \frac{\partial}{\partial z} \left(\frac{\phi_0}{\overline{u} - c_0} \right)$$
$$= \left[(\overline{u} - c_0) \frac{\partial \phi_0}{\partial z} - \phi_0 \frac{\partial \overline{u}}{\partial z} \right] (\overline{u} - c_0)^{-2}. \quad (B.12)$$

Insertion of (B.5) into (B.10) yields the following expressions for the dust-modified correction to the frequency kc_{1r} and growth rate kc_{1i}:

$$kc_{1r} = \frac{1}{A_w} \frac{1}{k} \int_{-L/2}^{L/2} \int_0^\infty \overline{D} \frac{\rho}{\rho_0} \Lambda (-\phi_0^* P_{0z}) \overline{\alpha}_y \, dz' \, dy'$$
$$+ \frac{1}{A_w} \frac{1}{k} \int_{-L/2}^{L/2} \int_0^\infty \overline{D} \frac{\rho}{\rho_0} \frac{f_0}{N^2} \Lambda |P_{0z}|^2 (\overline{u} - c_0)^2 \overline{\alpha}_z \, dz' \, dy', \quad (B.13a)$$

and

$$kc_{1i} = \frac{1}{A_w} \int_{-L/2}^{L/2} \int_0^\infty \frac{\rho}{\rho_0} \Lambda[-\phi_0^* P_{0z}(\overline{u} - c_0)]\overline{\alpha}_y \, dz' \, dy'$$

$$+ \frac{1}{A_w} \int_{-L/2}^{L/2} \int_0^\infty \frac{\rho}{\rho_0} \frac{f_0}{N^2} \Lambda |P_{0z}|^2 (\overline{u} - c_0)^3 \overline{\alpha}_z \, dz' \, dy',$$

$$\text{(B.13b)}$$

where

$$\Lambda = \delta[(\overline{u} - c_0)^2 + (\overline{D}/k)^2]^{-1} \quad \text{and} \quad \text{(B.14)}$$

$$(\overline{\alpha}_y, \overline{\alpha}_z) = \left(\overline{\Gamma} \frac{\partial \overline{\gamma}}{\partial y}, \ \overline{\Gamma} \frac{\partial \overline{\gamma}}{\partial z} \right). \quad \text{(B.15)}$$

Insertion of (B.12) into (B.13a) and (B.13b) and rearranging terms yields the frequency and growth-rate expressions (2.11a) and (2.11b) in section 2b.

REFERENCES

Afiesimama, E. A., 2007: Annual cycle of the mid-tropospheric easterly jet over West Africa. *Theor. Appl. Climatol.*, **90**, 103–111, doi:10.1007/s00704-006-0284-y.

Bender, C. M., and S. A. Orszag, 1978: *Advanced Mathematical Methods for Scientists and Engineers.* McGraw Hill, 593 pp.

Carlson, T. N., and C. B. Benjamin, 1980: Radiative heating rates for Saharan dust. *J. Atmos. Sci.*, **37**, 193–213, doi:10.1175/1520-0469(1980)037<0193:RHRFSD>2.0.CO;2.

Charney, J. G., and M. E. Stern, 1962: On the stability of internal baroclinic jets in a rotating atmosphere. *J. Atmos. Sci.*, **19**, 159–172, doi:10.1175/1520-0469(1962)019<0159:OTSOIB>2.0.CO;2.

Chen, S.-H., J. Dudhia, J. S. Kain, T. Kindap, and E. Tan, 2008: Development of the online MM5 tracer model and its applications to air pollution episodes in Instanbul, Turkey, and Sahara dust transport. *J. Geophys. Res.*, **113**, D11203, doi:1029/2007JD009244.

——, S.-H. Wang, and M. Waylonis, 2010: Modification of Saharan air layer and environmental shear over the eastern Atlantic Ocean by dust-radiation effects. *J. Geophys. Res.*, **115**, D21202, doi:10.1029/2010JD014158.

——, Y.-C. Liu, T. R. Nathan, C. Davis, R. Torn, N. Sowa, C.-T. Cheng, and J.-P. Chen, 2015: Modeling the effects of dust-radiative forcing on the movement of Hurricane *Helene* (2006). *Quart. J. Roy. Meteor. Soc.*, **141**, 2563–2570, doi:10.1002/qj.2542.

Cho, H.-R., and M. A. Jenkins, 1987: The thermal structure of tropical easterly waves. *J. Atmos. Sci.*, **44**, 2531–2539, doi:10.1175/1520-0469(1987)044<2531:TTSOTE>2.0.CO;2.

Chou, M. D., and M. J. Suarez, 1999: A solar radiation parameterization for atmospheric studies. Vol. 15, Technical Report Series on Global Modeling and Data Assimilation, NASA Tech. Memo. NASA/TM-1999-104606, 51 pp. [Available online at https://ntrs.nasa.gov/archive/nasa/casi.ntrs.nasa.gov/19990060930.pdf.]

——, ——, X. Z. Liang, and M. M. H. Yan, 2001: A thermal infrared radiation parameterization for Atmospheric Studies. Vol. 15, Technical Report Series on Global Modeling and Data Assimilation, NASA Tech. Memo. NASA/TM-1999-104606, 68 pp. [Available online at https://ntrs.nasa.gov/archive/nasa/casi.ntrs.nasa.gov/20010072848.pdf.]

Cuesta, J., J. H. Marsham, D. J. Parker, and C. Flamant, 2009: Dynamical mechanisms controlling the vertical redistribution of dust and the thermodynamic structure of the West Saharan atmospheric boundary layer during summer. *Atmos. Sci. Lett.*, **10**, 34–42, doi:10.1002/asl.207.

Echols, R. S., and T. R. Nathan, 1996: Effect of ozone heating on forced equatorial waves. *J. Atmos. Sci.*, **53**, 263–275, doi:10.1175/1520-0469(1996)053<0263:EOOHOF>2.0.CO;2.

Edmon, H. J., B. J. Hoskins, and M. E. McIntyre, 1980: Eliassen–Palm cross sections for the troposphere. *J. Atmos. Sci.*, **37**, 2600–2616, doi:10.1175/1520-0469(1980)037<2600:EPCSFT>2.0.CO;2.

Engelstaedter, S., and R. Washington, 2007: Atmospheric controls on the annual cycle of North African dust. *J. Geophys. Res.*, **112**, D03103, doi:10.1029/2006JD007195.

Ghan, S. J., 1989a: Unstable radiative dynamical interactions. Part I: Basic theory. *J. Atmos. Sci.*, **46**, 2528–2543, doi:10.1175/1520-0469(1989)046<2528:URIPIB>2.0.CO;2.

——, 1989b: Unstable radiative dynamical interactions. Part II: Expanded theory. *J. Atmos. Sci.*, **46**, 2544–2561, doi:10.1175/1520-0469(1989)046<2544:URDIPI>2.0.CO;2.

Grogan, D. F. P., T. R. Nathan, R. S. Echols, and E. C. Cordero, 2012: A parameterization for the effects of ozone on the wave driving exerted by equatorial waves in the stratosphere. *J. Atmos. Sci.*, **69**, 3715–3731, doi:10.1175/JAS-D-11-0343.1.

——, ——, and S.-H. Chen, 2016: Effect of Saharan dust on the linear dynamics of African easterly waves. *J. Atmos. Sci.*, **73**, 891–911, doi:10.1175/JAS-D-15-0143.1.

——, ——, and ——, 2017: Saharan dust and the nonlinear evolution of the African easterly jet–African easterly wave system. *J. Atmos. Sci.*, **74**, 27–47, doi:10.1175/JAS-D-16-0118.1.

Hall, N. M. J., G. N. Kiladis, and C. D. Thorncroft, 2006: Three-dimensional structure and dynamics of African easterly waves. Part II: Dynamical modes. *J. Atmos. Sci.*, **63**, 2231–2245, doi:10.1175/JAS3742.1.

Hess, M., P. Koepke, and I. Shult, 1998: Optical properties of aerosols and clouds: The software package OPAC. *Bull. Amer. Meteor. Soc.*, **79**, 831–844, doi:10.1175/1520-0477(1998)079<0831:OPOAAC>2.0.CO;2.

Jones, C., N. Mahowald, and C. Luo, 2003: The role of easterly waves on African desert dust transport. *J. Climate*, **16**, 3617–3628, doi:10.1175/1520-0442(2003)016<3617:TROEWO>2.0.CO;2.

——, ——, and ——, 2004: Observational evidence of African desert dust intensification of easterly waves. *Geophys. Res. Lett.*, **31**, L17208, doi:10.1029/2004GL020107.

Jury, M. R., and M. J. Santiago, 2010: Composite analysis of dust impacts on African easterly waves in the Moderate Resolution Imaging Spectrometer era. *Geophys. Res. Lett.*, **115**, D16213, doi:10.1029/2009JD013612.

Karyampudi, V. M., and T. N. Carlson, 1988: Analysis and numerical simulations of the Saharan air layer and its effect on easterly wave disturbances. *J. Atmos. Sci.*, **45**, 3102–3136, doi:10.1175/1520-0469(1988)045<3102:AANSOT>2.0.CO;2.

Kaufman, Y. J., I. Koren, L. A. Remer, D. Tanré, P. Ginoux, and S. Fan, 2005: Dust transport and deposition observed from Terra-Moderate Resolution Imaging Spectroradiometer (MODIS) spacecraft over the Atlantic Ocean. *J. Geophys. Res.*, **110**, D10S12, doi:10.1029/2003JD004436.

Kiladis, G. N., C. D. Thorncroft, and N. M. J. Hall, 2006: Three-dimensional structure and dynamics of African easterly waves. Part I: Observations. *J. Atmos. Sci.*, **63**, 2212–2230, doi:10.1175/JAS3741.1.

Knippertz, P., and M. C. Todd, 2010: The central west Saharan dust hot spot and its relation to African easterly waves and extratropical disturbances. *J. Geophys. Res.*, **115**, D12117, doi:10.1029/2009JD012819.

Kok, J. F., 2011: A scaling theory for the size distribution of emitted dust aerosols suggests climate models underestimate the size of the global dust cycle. *Proc. Natl. Acad. Sci. USA*, **108**, 1016–1021, doi:10.1073/pnas.1014798108.

Leroux, S., and N. M. J. Hall, 2009: On the relationship between African easterly waves and the African easterly jet. *J. Atmos. Sci.*, **66**, 2303–2316, doi:10.1175/2009JAS2988.1.

——, ——, and G. N. Kiladis, 2011: Intermittent African easterly wave activity in a dry atmospheric model: Influence of the extratropics. *J. Climate*, **24**, 5378–5396, doi:10.1175/JCLI-D-11-00049.1.

Liou, K. N., 2002: *An Introduction to Atmospheric Radiation*, Academic Press, 583 pp.

Ma, P.-L., K. Zhang, J. J. Shi, T. Matsui, and A. Arking, 2012: Direct radiative effect of mineral dust on the development of African easterly waves. *J. Appl. Meteor. Climatol.*, **51**, 2090–2104, doi:10.1175/JAMC-D-11-0215.1.

Miller, R. L., and I. Tegen, 1998: Climate response to soil dust aerosols. *J. Climate*, **11**, 3247–3267, doi:10.1175/1520-0442(1998)011<3247:CRTSDA>2.0.CO;2.

——, P. Knippertz, C. P. García-Pando, J. P. Perlwitz, and I. Tegen, 2014: Impact of dust-radiative forcing upon climate. *Mineral Dust: A Key Player in the Earth System*, P. Knippertz and J.-B. W. Stuut, Eds., Springer Science, 327–357, doi:10.11007/978-94-017-8978-3_13.

Nathan, T. R., 1989: On the role of ozone in the stability of Rossby normal modes. *J. Atmos. Sci.*, **46**, 2094–2100, doi:10.1175/1520-0469(1989)046<2094:OTROOI>2.0.CO;2.

——, and L. Li, 1991: Linear stability of free planetary waves in the presence of radiative–photochemical feedbacks. *J. Atmos. Sci.*, **48**, 1837–1855, doi:10.1175/1520-0469(1991)048<1837:LSOFPW>2.0.CO;2.

——, and D. Hodyss, 2010: Troposphere–stratosphere communication through local vertical waveguides. *Quart. J. Roy. Meteor. Soc.*, **136**, 12–19, doi:10.1002/qj.532.

Pedlosky, J., 1987: *Geophysical Fluid Dynamics*. Springer, 710 pp.

Prospero, J. M., 1999: Long-range transport of mineral dust in the global atmosphere: Impact of African dust on the environment of the southeastern United States. *Proc. Natl. Acad. Sci. USA*, **96**, 3396–3403, doi:10.1073/pnas.96.7.3396.

——, and T. N. Carlson, 1972: Vertical and areal distributions of Saharan dust over the western equatorial North Atlantic Ocean. *J. Geophys. Res.*, **77**, 5255–5265, doi:10.1029/JC077i027p05255.

Pytharoulis, I., and C. Thorncroft, 1999: The low-level structure of African easterly waves in 1995. *J. Atmos. Sci.*, **127**, 2266–2280, doi:10.1175/1520-0493(1999)127<2266:TLLSOA>2.0.CO;2.

Reed, R. J., A. Hollingsworth, W. A. Heckley, and F. Delsol, 1988: An evaluation of the performance of the ECMWF Operational System in analyzing and forecasting easterly wave disturbances over Africa and the tropical Atlantic. *Mon. Wea. Rev.*, **116**, 824–865, doi:10.1175/1520-0493(1988)116<0824:AEOTPO>2.0.CO;2.

Rennick, M. A., 1976: The generation of African waves. *J. Atmos. Sci.*, **33**, 1955–1969, doi:10.1175/1520-0469(1976)033<1955:TGOAW>2.0.CO;2.

Simmons, A. J., 1977: A note on the instability of the African easterly jet. *J. Atmos. Sci.*, **34**, 1670–1674, doi:10.1175/1520-0469(1977)034<1670:ANOTIO>2.0.CO;2.

Thorncroft, C. D., 1995: An idealised study of African easterly waves. III: More realistic basic states. *Quart. J. Roy. Meteor. Soc.*, **121**, 1589–1614, doi:10.1002/qj.49712152706.

——, and B. J. Hoskins, 1994: An idealized study of African easterly waves. I: Linear theory. *Quart. J. Roy. Meteor. Soc.*, **120**, 953–982, doi:10.1002/qj.49712051809.

——, N. M. J. Hall, and G. N. Kiladis, 2008: Three-dimensional structure and dynamics of African easterly waves. Part III: Genesis. *J. Atmos. Sci.*, **65**, 3596–3607, doi:10.1175/2008JAS2575.1.